MICROSTRUCTURAL EVOLUTION IN CAST HAYNES 282 FOR APPLICATION IN ADVANCED POWER PLANTS

Y. Yang[1] and R. C. Thomson[1]

[1]Department of Materials, Loughborough University, Loughborough, Leicestershire, LE11 3TU, UK

R. M. Leese[2] and S. Roberts[2]

[2]Goodwin Steel Castings Limited, Ivy House Foundry, Ivy House Road, Hanley, Stoke-on-Trent, Staffordshire, ST1 3NR, UK

ABSTRACT

There is a worldwide drive to increase the efficiency of power plants in order to reduce the amount of fossil fuel consumed and associated CO_2 emissions. Raising the operating temperature and pressure can improve the thermal efficiency, however, this necessitate the use of materials which have high temperature performance. Steels are currently used at temperature up to 600°C with the efficiency of 38-40 %. Advanced Ultra Supercritical (A-USC) design plans power plants to operate at steam temperatures of 700°C and pressure up to 35 MPa with a lifetime of at least 100 000 hours. Ni-base superalloys are leading materials due to their significant strength and creep resistance.

Haynes 282 is one possible candidate to meet the A-USC conditions for turbine engines. This alloy is a γ' precipitation strengthened material and exhibits very good creep properties and thermal stability. The alloy examined in this research was produced by sand casting, and therefore the aim of this research is to investigate the microstructural evolution in large scale cast components.

The alloy has been examined in both the as-cast condition and as a function of a range of different pre-service heat treatments. The microstructural changes during different heat treatments have been fully identified and quantified. The results have also been compared with predictions from thermodynamic equilibrium calculations using a Ni alloy database. It has been found that variations in the heat treatment conditions can have a significant effect on microstructural development and hence, potentially, the mechanical properties of Haynes 282 alloy.

1 INTRODUCTION

Haynes 282 was first introduced in 2005 as an advanced wrought gamma prime strengthened superalloy for high temperature applications such as aircraft and land based gas turbines [1]. It is notable for its exceptional high temperature creep strength, good weldability and fabricability and its resistance to strain-age cracking [1].

After fabrication, wrought Haynes 282 materials often undergo a standard heat treatment: a solution annealing treatment followed by quenching and then a two-stage precipitation treatment with air cooling to achieve optimum mechanical properties [1, 2]. The solution annealing temperature is designed to be above the solvus of $M_{23}C_6$ to make the material soft and ductile [2]. The first precipitation treatment temperature is above the solvus of gamma-prime and it is designed to precipitate out $M_{23}C_6$ both intergranularly and intragranularly to give optimum creep strength and high temperature ductility [2]. The second precipitation treatment is designed to form γ' to strengthen the material [2].

It is well known that there are many phases present in Ni-based superalloys, including different carbides and TCP phases [3] and that these phases can have different effects on mechanical properties. It has been reported that the microstructure of the heat treated Haynes 282 contains MC carbide, Cr rich $M_{23}C_6$ both intergranularly and intragranularly, and also a uniform distribution of spherical γ′ particles with a typical size of 20 nm [2].

There are a number of studies in the literature concerned with the microstructure of Haynes 282, particularly focused on welds [4-8]. One study of the fusion zone in a laser weld of Haynes 282 observed that Co, Cr and Al were homogeneously distributed between the dendrite core and interdendritic regions, whereas the Ti and Mo were rejected to the interdendritic region and formed Ti-Mo rich, MC type carbides [6]. Three types of particles have also been identified along the grain boundaries in Haynes 282 weld metal which were Cr-rich, Mo-rich and Ti-rich [8]. It was also observed that there was B peak in the Mo-rich particle, and it was suggested that the Mo-rich phases are M_5B_3 with lattice parameter of a=0.56 nm and c=1.01 nm [8]. There are reports of other borides present in the alloy [5], including Ni–rich, Cr-rich and Mo-rich borides of the form M_3B_2. Additionally, it has been reported the grain boundaries were covered by both $M_{23}C_6$ and M_5B_3 [4, 7]. However, other authors [9] have also found a Mo rich phase before precipitation treatment which was also associated with C and Si peaks, and they postulated that the Mo rich phase was M_6C. Therefore, it is still necessary to undertake a detailed microstructural study of Haynes 282, and in particular most of the literature is focussed on the wrought alloy. This research therefore is concerned with a full microstructural investigation of cast Haynes 282 in various heat treated conditions with possible application for heavy sections in the power sector.

2 MATERIALS AND EXPERIMENTAL PROCEDURES

The material studied in this research was produced by Goodwin Steel Castings Limited using sand casting. The material examined was cut from the feeder part of a large cast section. The nominal composition of Haynes 282 is given in Table 1. The initial solution heat treatment was slightly modified to allow for the fact that this was a large casting rather than a wrought alloy, with a two-stage solution treatment being applied comprising of 1100°C for 6 hrs and then a ramp up to 1150°C for 15 hrs followed by water quenching. After the solution treatment, a two-stage ageing treatment was applied which was the same as the standard Haynes precipitation treatment but with a longer holding time at 1010°C for 5 hrs followed by quenching, and then a second ageing treatment at 788°C for 15 hrs followed by air cooling.

Eight samples cut from the cast 282 material were examined in this paper and their condition and code names are provided in Table 2. The material was examined in the as cast condition (AC) for comparison purposes, then after solution treatment (ST), after the first stage aged condition (ST-FA), and after solution treatment and both aged conditions for different ageing times of the second ageing treatment: 15 hrs, 100 hrs, 1000 hrs, 2000 hrs and 3000 hrs (ST-FA-SA** where ** indicates the length of the heat treatment). Samples were cut to a suitable size and then mounted in conducting Bakelite. Mounted samples were ground on SiC papers from 220 to 1200 grit, and then polished with 9, 3, 1 μm diamond solution and finally polished with colloidal silica (0.5 μm) for 30 min. To quantify gamma prime, the etchant Kallings no.2 ($CuCl_2$-2g, HCL-40 ml and ethanol-40-80 ml) was used for 10 s to highlight the γ′. The Vickers hardness of all samples were measured by a Mitutoyo HM-124 machine using a 10 kg load and a 15 s dwell time. For each sample, ten measurements were performed and the average value was taken.

Table 1: The nominal composition in wt. % of Haynes 282

C	Cr	Mo	Si	Ti	Co	B	Al	Ni
0.06	20	8.5	0.15	2.1	10	0.005	1.5	Bal.

Table 2: Conditions and code names of all the samples in this paper. The solution treatment was carried out at 1100°C for 6 hrs, followed by a ramp to 1150°C for 15 hrs and water quenched. First ageing was carried out at 1010°C for 5 hrs followed by water quenching, and the second ageing was at 788°C for various times followed by air cooling.

Sample name	Heat treatment condition			
	As Cast	Solution Treated	First Aged	Second Aged
AC	√			
ST	√	√		
ST-FA	√	√	√	
ST-FA-SA15	√	√	√	15 hrs
ST-FA-SA100	√	√	√	100 hrs
ST-FA-SA1000	√	√	√	1000 hrs
ST-FA-SA2000	√	√	√	2000 hrs
ST-FA-SA3000	√	√	√	3000 hrs

Thermodynamic calculations were performed using the MTDATA [10] software developed by the National Physical Laboratory with an appropriate Ni-database [11]. The alloy composition was used to predict the equilibrium phases between 300-1600°C and the chemical composition of each phase as a function of temperature. Solidification and chemical segregation profiles were also predicted using the Scheil methodology (Tscheil).

Different microstructural features were assessed using a Carl Zeiss (Leo) 1530 VP field emission fun scanning electron microscope (FEG-SEM). The backscatter mode was used to show different phases due to its atomic number contrast. Energy dispersive X-ray (EDS) analysis was also used for chemical analysis, with an operating voltage of 20 kV. Transmission electron microscopy (TEM) was used to study small precipitates. A JEOL 2000FX TEM was used to obtain the diffraction patterns of different precipitates and an fei F20 Tecnai FEG-TEM was used to obtain EDS maps and spectra of different small precipitates. The site specific TEM samples were prepared using an fei Nova Nanolab 600 dual beam which consists of a field emission electron column and a gallium source ion column.

3 RESULTS AND DISCUSSION

3.1 Thermodynamic calculations

The calculated equilibrium phase diagram is illustrated in Figure 2. The phases considered in the calculation were liquid, gamma, gamma prime, MX, $M_{23}C_6$, M_6C, M_3B_2 and Mu. From Figure 2 (a), it can be seen that the predicted melting range is from 1300°C to 1380°C. Gamma prime forms below 1000°C and nearly 20 wt. % is precipitated at 788°C, which is the standard second ageing treatment temperature. The magnified phase diagram of the precipitates present in smaller quantities, including MX, M_6C, $M_{23}C_6$ and M_3B_2, is illustrated in Figure 2 (b). It can be seen that MX is present until melting, and M_3B_2 and $M_{23}C_6$ precipitate out below 1250°C and 800°C respectively. It should be noticed that M_6C is present between 780°C to 1080°C. This is because below 780°C, the $M_{23}C_6$ is more stable [3].

The equilibrium composition of the different precipitates including gamma prime, MX, M_6C, $M_{23}C_6$, M_3B_2, and Mu were also predicted as illustrated in Figure 3. It can be seen that MX is a Ti rich carbon nitride and $M_{23}C_6$ is Cr rich. It should be noted that the M_6C, M_3B_2 and Mu phases are all Mo rich, however, M_6C is Mo and Ni rich, M_3B_2 is Mo and Cr rich and the Mu phase is Mo and Co rich.
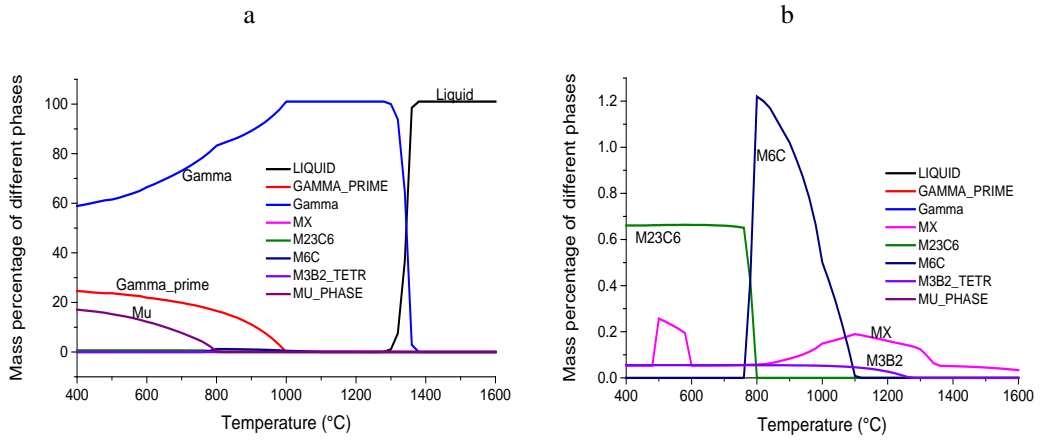
Figure 2: Plots of the equilibrium phase diagram of the Haynes 282 (a) and at a magnified scale for the minor precipitate phases M_6C, $M_{23}C_6$, M_3B_2 and MX (b).
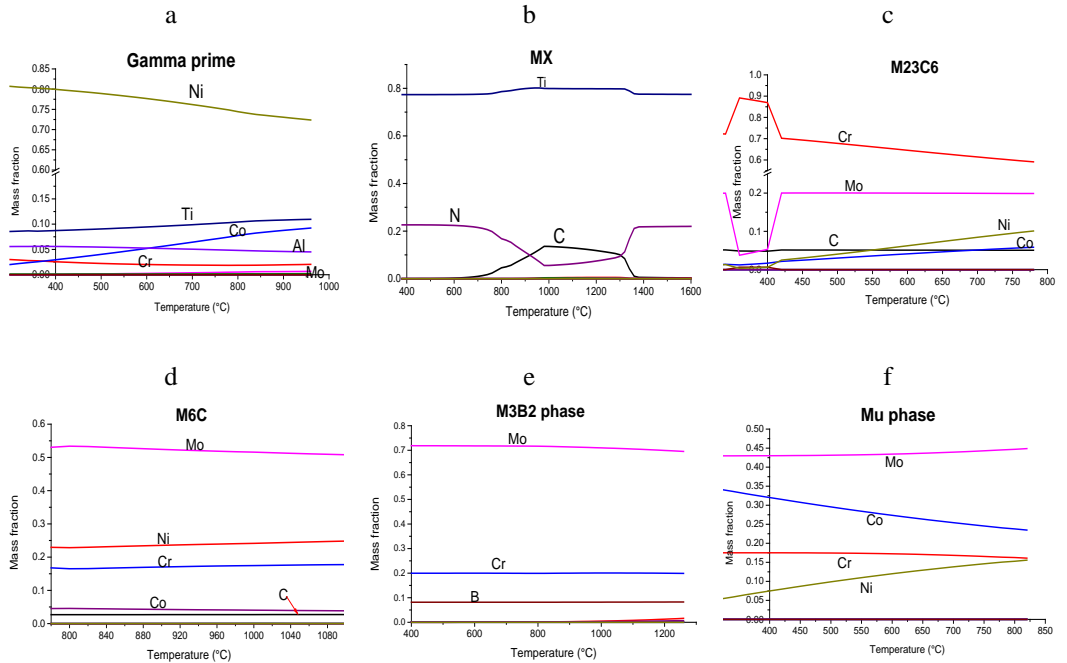

Figure 3: Plots of the calculated equilibrium composition of different phases: (a) gamma prime; (b) MX; (c) $M_{23}C_6$; (d) M_6C; (e) M_3B_2; and (f) Mu

Since segregation is a normal phenomenon during casting, Scheil calculations have also been carried out and the results are illustrated in Figure 4. From the phase diagram in Figure 4 it can be seen that the solidification sequence in the Haynes 282 is gamma, MX, M_6C, M_3B_2, Mu and gamma prime. M_6C is present from 1250°C to 1175°C, then M_3B_2 forms and followed by Mu phase. From Figure 4 (b), it can be seen that there is a relatively high amount of MX which forms together with gamma at the start of solidification, and Figure 4 (c) shows that the initial MX is rich in nitrogen, a Ti rich carbonitride whereas later it becomes a Ti, Nb rich carbide. This is very similar to the equilibrium prediction but with much more Nb and Mo due to segregation. Figure 5

illustrates the segregation ratio of elements in the liquid during solidification and it is obvious that Nb and B are most heavily segregated, together with Ti and Mo.
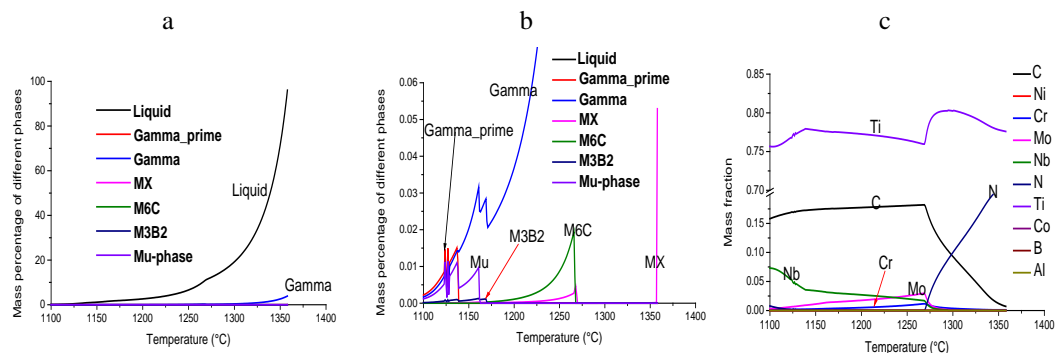

Figure 4: Predictions from Tscheil calculations: (a) phase diagram; (b) enlarged phase diagram for MX, M₆C, M₃B₂, Mu and gamma prime; (c) predicted composition of MX formed during solidification
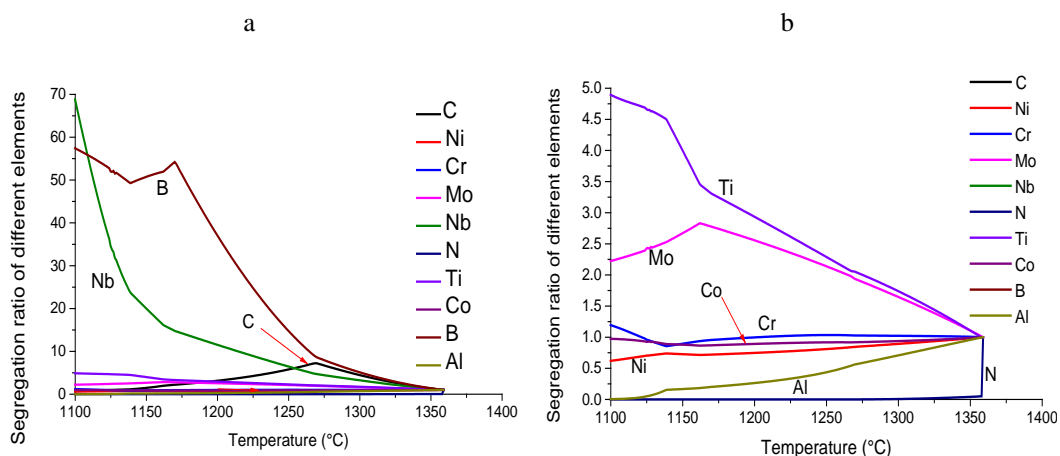

Figure 5: Tscheil calculation predicted plots of segregation ratio of elements in liquid during solidification (a) and the enlarged plot for C, Ti, Mo, Ni, Co, Cr and Al (b)

3.2 Hardness

The results from hardness testing of all samples are shown in Figure 6. It can be seen that the AC sample has a higher hardness than the ST sample, which in turn has the lowest overall hardness as a result of the dissolution of all of the strengthening precipitates. The AC sample was observed to contain some gamma prime, as indicated in Figure 4 (b). After first and second ageing, the hardness increased by up to ~160 HV compared to the solution treated sample. However, it was noted that the ST-FA sample was ~40 HV higher than the ST sample in hardness, implying that this increase in hardness is a result of precipitation during the first ageing. Therefore, in comparing the hardness of the FA and SA samples, it can be inferred that gamma prime results in ~120 HV strengthening. Comparing the second ageing samples, it can be seen that the ST-FA-SA1000 sample and the ST-FA-SA2000 sample approach the highest hardness with very similar values. The absolute values of hardness are a function of both the amount and size distribution of

gamma prime. It was, however, observed that the hardness of the ST-FA-SA3000 sample was lower than the other aged samples, which could be caused by the coarsening of the gamma prime distribution, as discussed further in section 3.5.
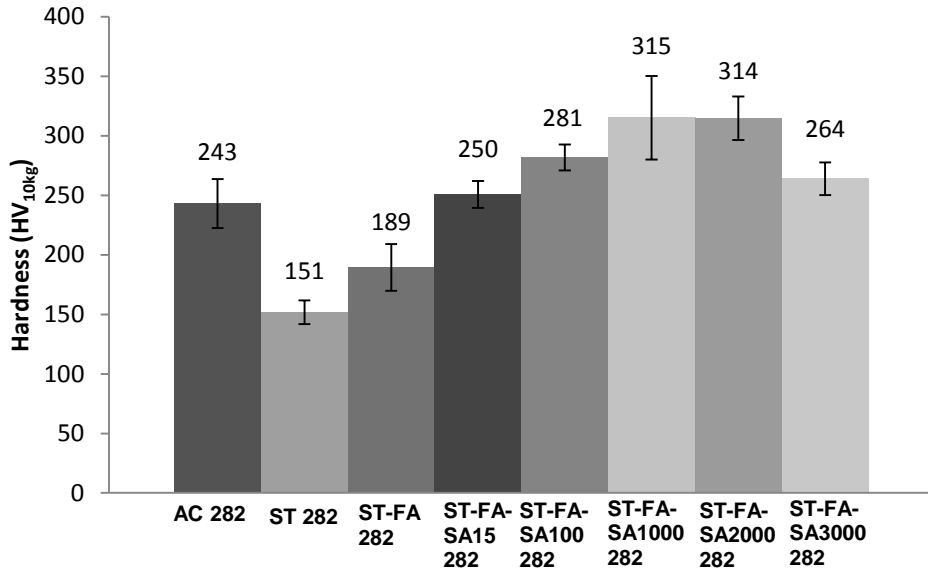

Figure 6: A plot showing the hardness of all of the samples examined in this research.

3.3 MX precipitates

Two types of MX precipitates were found in the AC condition: one was a Ti rich nitride with a cubic morphology as shown in Figure 7 (a) and the other was a Ti, Mo rich carbide with a blocky morphology along grain boundaries (Figure 7b). These results are in agreement with the predicted composition of MX in the segregated state, as presented in Figure 4 (c). The diffraction pattern of the cubic TiN illustrated in Figure 7 (a) is consistent with an FCC structure with a lattice parameter of 0.425 nm, and the diffraction pattern of the blocky boundary (Ti,Mo)C illustrated in Figure 7 (b) indicates that the (Ti,Mo)C phase also has an FCC structure with a lattice parameter of 0.432 nm. Compared to TiN, the increase in lattice parameter of the (Ti,Mo)C is caused by the larger substitutional atom, Mo, substituting for Ti.

After the solution treatment, the blocky (Ti,Mo)C particles disappeared and instead complex MX particles formed comprising TiN surrounded by (Ti,Mo)C, as illustrated in Figure 8, which shows the morphology of the complex MX in different aged conditions. It can be seen that the complex MX were stable during subsequent ageing treatments. However, it should be noticed that after the first ageing treatment, white precipitates were observed around the complex MX. From the equilibrium phase diagram, the white precipitates could be M_6C or M_3B_2. However, the solvus of M_3B_2 is above the solution treatment temperature and it was not observed in the ST sample. Therefore the white precipitates are more likely to be M_6C, as discussed in section 3.4, and were observed to coarsen slightly during the second ageing treatment with increasing ageing time.
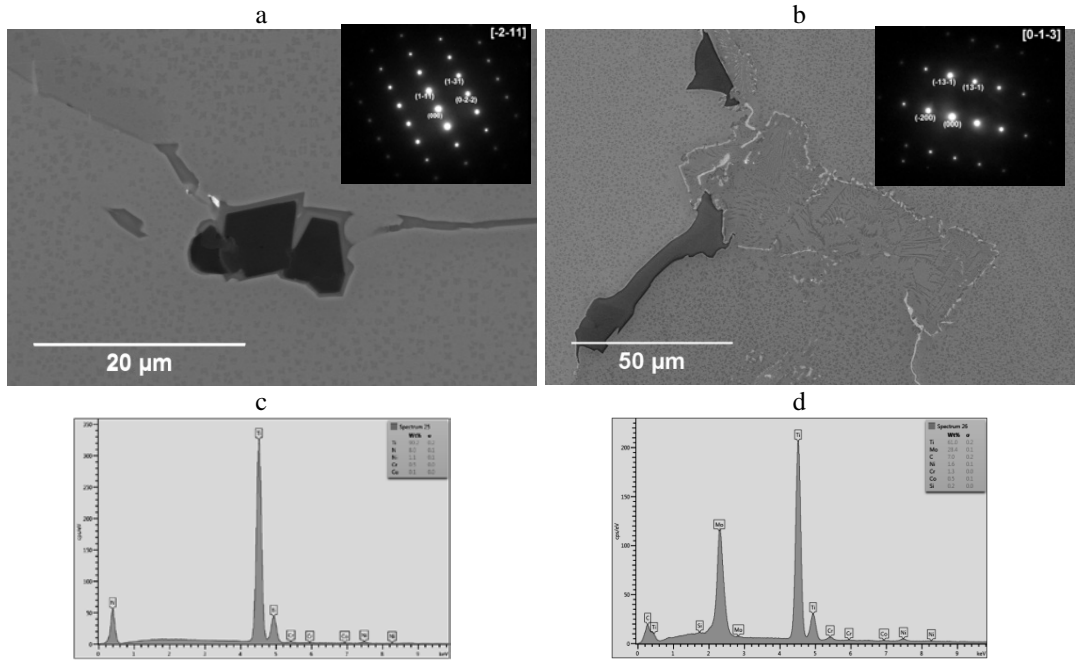
Figure 7: Micrographs of the microstructure of the AC sample: (a) cubic TiN surrounded by (Ti,Mo)C on a grain boundary and the diffraction pattern of the TiN, zone axis [-2-11]; (b) blocky (Ti,Mo)C along a grain boundary and its diffraction pattern, zone axis [0-1-3]; (c) a EDS spectrum of the TiN; and (d) a EDS spectrum of the (Ti,Mo)C
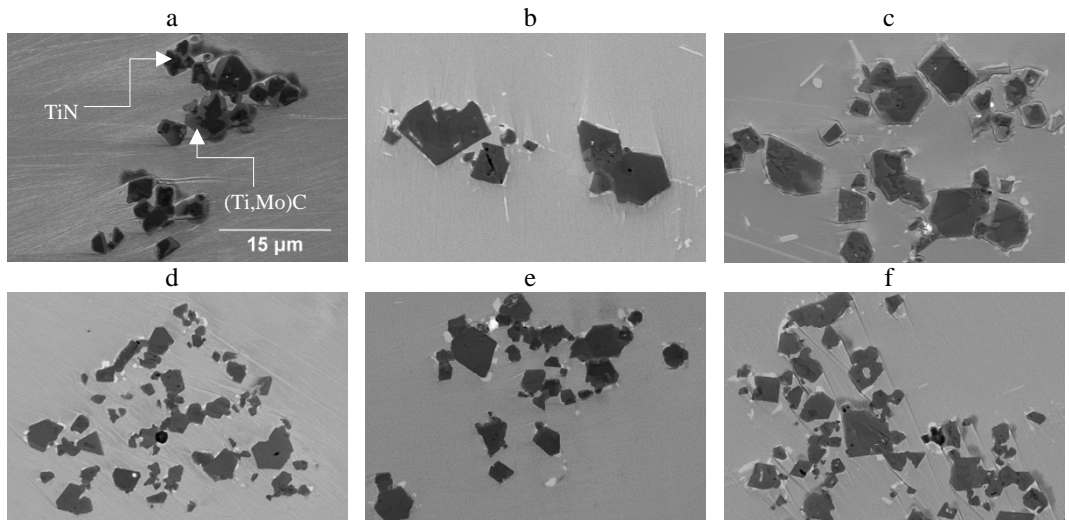

Figure 8: Micrographs of the heat treated samples: (a) the ST sample; (b) the ST-FA sample; (c) the ST-FA-SA15 sample (d) the ST-FA-SA100 sample; (d) the ST-FA-SA1000 sample and (f) the ST-FA-SA2000 sample.

3.4 Boundary precipitates

Two types of grain boundary precipitates were found in the AC condition as shown in Figure 9 (a). The EDS spectra in Figure 9 (b and c) indicated that the white precipitates were Mo, Si rich carbide and the dark precipitates were Cr rich carbides. The diffraction patterns of the dark precipitate in Figure 9 (f and g) show an FCC structure with a lattice parameter of 1.06 nm. Therefore, it can be concluded that the Cr rich dark precipitates are Cr rich $M_{23}C_6$. From the equilibrium composition diagram in Figure 3, it can be seen that the Mo containing phases are M_6C, M_3B_2 or Mu. The diffraction patterns of the white precipitates in Figure 9 (d and e) show a diamond cubic structure with a lattice parameter of 1.10 nm. However, M_3B_2 has a primitive tetragonal structure, where lattice parameters a and c are 0.59 and 0.31 nm respectively [12] and Mu has a rhombohedral structure where lattice parameters a and c are 0.9 and 3.08 nm respectively [13]. Therefore, the boundary white precipitates are consistent with M_6C.
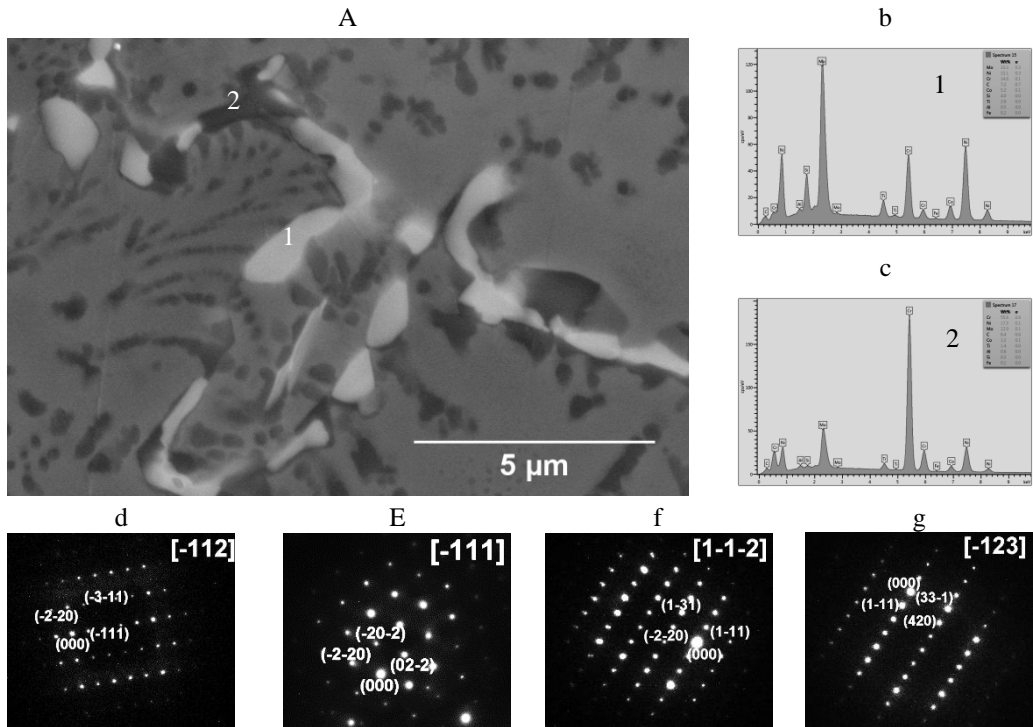

Figure 9: A micrograph of the grain boundary in the AC sample (a); (b) a spectrum from the white precipitate; (c) a spectrum from the dark precipitate; (d and e) the diffraction patterns of the white precipitate with zone axis [-112] and [-111] respectively and (f and g) the diffraction patterns of the dark precipitate with zone axis [1-1-2] and [-123] respectively

After the solution treatment both boundary precipitates were dissolved, as illustrated in Figure 10 (a). It can be seen that there are only complex MX particles in the grain boundaries in the ST sample. This is because the solution treatment temperatures are above the solvus of both M_6C and $M_{23}C_6$. The disappearance of the M_6C after the solution treatment also provides further evidence that the white precipitates are not M_3B_2 since the solvus of the M_3B_2 is above the solution treatment temperature. During the first ageing treatment, M_6C re-precipitated and covered the grain boundaries again as seen in Figure 10 (b). From the equilibrium phase diagram in Figure 2 (b), it can be seen that at 1010°C, the microstructure is predicted to comprise gamma, MX and M_6C, which is consistent with those observed in the microstructure of the ST-FA sample. After the second ageing treatment, $M_{23}C_6$ re-precipitated and covered the grain boundaries, together with M_6C, as shown in Figure 10 (c). A specific lift out sample of the grain boundary in the ST-

FA-SA15 was made and EDS maps from the FEG-TEM also proved the grain boundaries were covered by alternating Mo and Cr rich carbides. Figure 11 shows micrographs of the ST-FA-SA samples after different ageing times. It can be seen that with the increasing ageing time at 788°C, both M_6C and $M_{23}C_6$ coarsened.
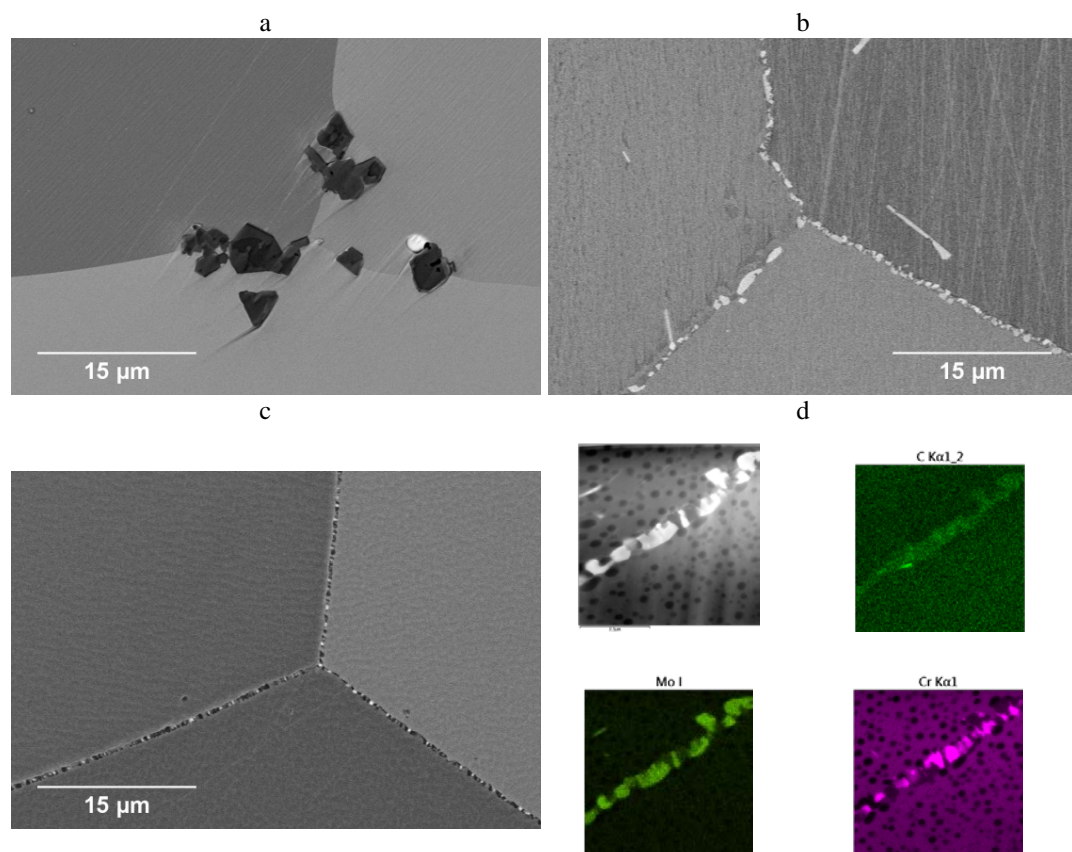

Figure 10: Micrographs of the grain boundary structure of different samples: (a) the ST sample; (b) the ST-FA sample; (c) the ST-FA-SA15 sample; (d) A TEM micrograph of a grain boundary in the ST-FA-SA15 sample and the corresponding EDS maps of Mo, Cr and C.
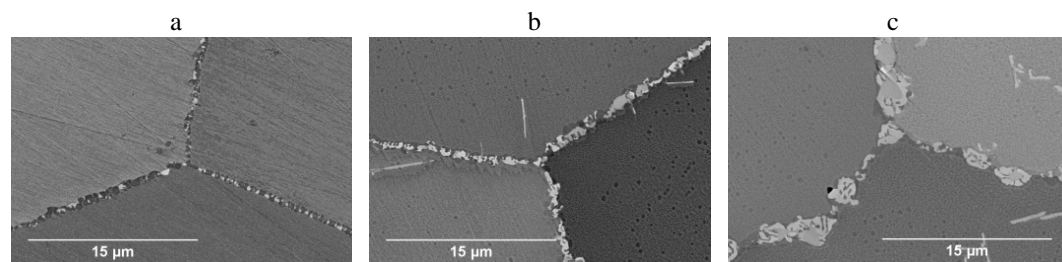

Figure 11: Micrographs of the grain boundary structure of different aged samples: (a) the ST-FA-SA100 sample; (b) the ST-FA-SA1000 sample and (c) the ST-FA-SA2000 sample

3.5 Gamma prime

Gamma prime has been found in the AC sample, in agreement with the predicted solidification sequence. It should be noticed that the gamma prime in the AC sample appeared as clusters of gamma prime particles in a star morphology, consistent with previous results [14]. The gamma prime particles were then observed to re-precipitate out during the second ageing treatment in a spherical morphology, as shown in Figure 12.

The coarsening behaviour of the gamma prime particles has been quantified by investigating their average size and distribution in each aged sample. Image analysis software was used to analyse 15 micrographs for each sample condition and a significant number of the particles were measured (over 5000) to ensure good statistical significance. The average size of the gamma prime in the ST-FA-SA100 sample, the ST-FA-SA1000 sample, the ST-FA-SA2000 sample and the ST-FA-SA3000 sample were 42 nm, 102 nm, 119 nm and 231 nm respectively. Figure 13 (a) illustrates the distribution of the gamma prime in the different aged samples, and it is obvious that the distribution of gamma prime broadened with increasing time. It should be noted that the average size in the ST-FA-SA1000 sample and the ST-FA-SA2000 sample are nearly the same, which may explain why the hardness of these two samples was very similar. However, the size of the gamma prime in the ST-FA-SA3000 sample is about twice that of the ST-FA-SA2000 sample, consistent with the drop in hardness observed. Figure 13 (b) illustrates the coarsening rate of the gamma prime. It can be seen that the result agrees with the growth rate $r^3 \propto t$ [15].

It was also noted that the morphology of the gamma prime was still spherical up to 3000 hrs ageing. It is known that spherical gamma prime has the smallest misfit with gamma, and this may explain why Haynes 282 has good creep properties.
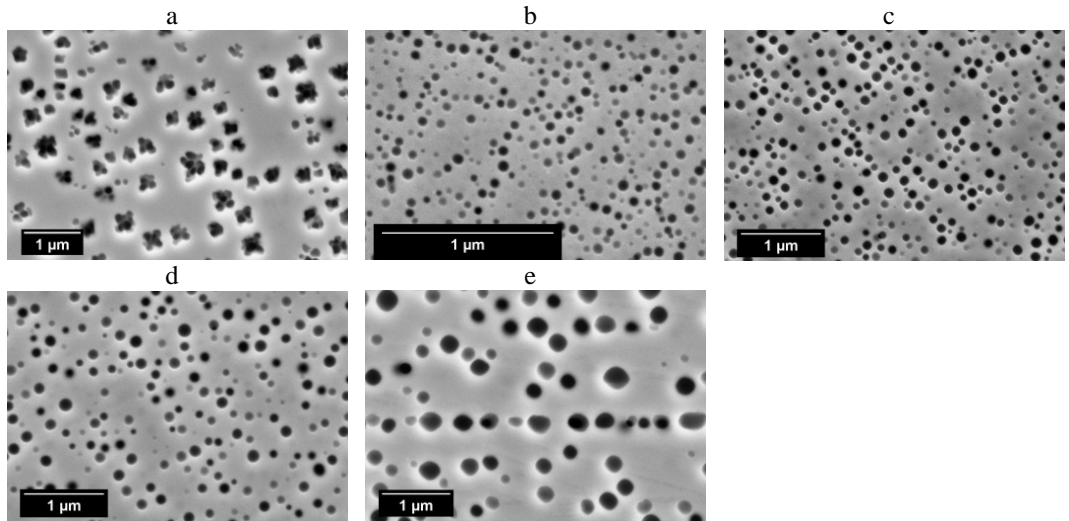

Figure 12: Micrographs of the gamma prime in different samples: (a) the AC sample; (b) the ST-FA-SA100 sample; (c) the ST-FA-SA1000 sample; (d) the ST-FA-SA2000 sample and (e) the ST-FA-SA3000 sample.
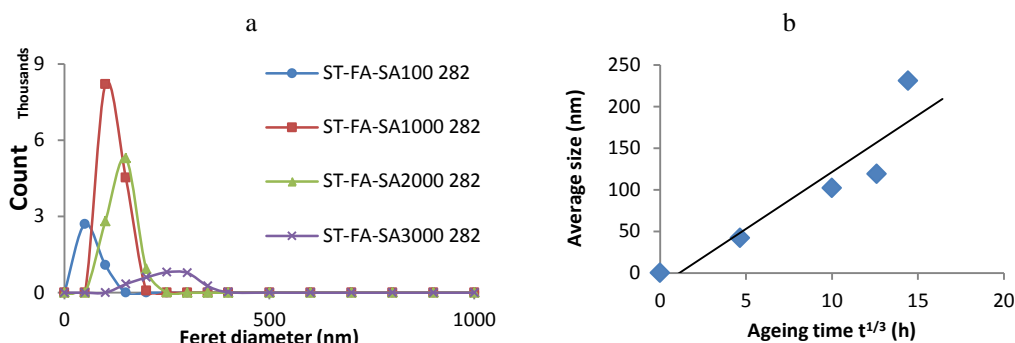
Figure 13: Plots showing the distribution of the gamma prime in the different aged samples (a) and the coarsening of the gamma prime (b).

4 CONCLUSIONS

Microstructural evolution of cast Haynes 282 has been fully studied using a number of analytical techniques, focusing on the different precipitates present. The observed phases present within the microstructures agreed well with the thermodynamic equilibrium and Scheil predictions.

In the AC condition, two types of MX were found, which were TiN and (Ti,Mo)C. $M_{23}C_6$, which is Cr rich and M_6C, which is Mo rich, were found to cover the grain boundaries. Gamma prime particles present in star morphology were also found in the AC sample, which had a relatively high hardness value of 243 HV.

After the solution treatment, the (Ti,Mo)C particles dissolved and formed a complex MX comprising TiN surrounded by (Ti,Mo)C. The other precipitates were all dissolved and thus the material was measure to have a significantly lower hardness value (151 HV).

M_6C was precipitated out during the first ageing treatment and covered the grain boundaries. This precipitation provided the material a hardness increase of 40 HV. During the second ageing treatment, $M_{23}C_6$ was precipitated and covered the grain boundaries, alternating with M_6C. With increasing ageing time, both $M_{23}C_6$ and M_6C coarsened. Spherical gamma prime particles were found during the second ageing treatment, and gave the material a maximum hardness increase of 120 HV. The coarsening of the gamma prime particles was observed to be proportional to time to the power one third. It should be noted that spherical gamma prime particles were found up to 3000 hrs, which could contribute to the alloy's relatively good creep properties.

5 ACKNOWLEDGEMENTS

6 REFERENCES

[1] Haynes 282 alloy Brochure, Online Literature, Haynes International, Inc. [Online] Access at: www.haynesintl.com/literature.htm

[2] Pike, L.M., "Development of Fabricable Gamma-prime (c9) Strengthened Superalloy," Proc. 11th Int. Symp. Superalloy 2008, Champion, PA, USA, September 2008, TMS, pp.191–200.

[3] Sims, C.T., Stoloff, N.S. and Hagel, W.C., Superalloy II, John Wiley & Sons (New York, 1987), pp. 101.

[4] Buckson, R.A. and Ojo, O.A., "Cyclic Deformation Characteristics and Fatigue Crack Growth Behaviour of a Newly Developed Aerospace Superalloy Haynes 282," Materials Science and Engineering A, Vol. 555, (2012), pp. 63-70.

[5] Ghoneim, A and Ojo, O.A., "Microstructure and Mechanical Response of Transient Liquid Phase Joint in Haynes 282 Superalloy," Materials Characterization, Vol. 62, (2012), pp.1-7.

[6] Osoba, L.O., Ding, R.G. and Ojo, O.A., "Microstructural Analysis of Laser Weld Fusion Zone in Haynes 282 Superalloy," Materials Characterization, Vol. 65, (2012), pp. 93-99.

[7] Osoba, L.O. and Ojo, O.A., "Influence of Laser Welding Heat Input on HAZ Cracking in Newly Developed Haynes 282," Materials Science and Technology, Vol. 28, No. 4, (2012), pp. 431-436.

[8] Osoba, L.O. and Ojo, O.A., "Improved Resistance to Laser Weld Heat-Affected Zone Microfissuring in a Newly Developed Superalloy Haynes 282," Metallurgical and Materials Transactions A, Vol. 43A, (2012), pp. 4281-4295.

[9] Boehlert, C.J. and Longanbach, S.C., "A Comparison of the Microstructure and Creep Behaviour of Cold Rolled Haynes 230 Alloy and Haynes 282 Alloy," Materials Science and Engineering A, Vol. 528, (2011), pp. 48888-4898.

[10] Davies, R.H., Dinsdale, A.T., Gisby, J.A., Robinson, J.A.J. and Martin, S.M., MTDATA-Thermodynamics and Phase Equilibrium Software from the National Physical Laboratory, (2002), pp. 229-271.

[11] Saunders, N., Proc. 8th Int. Symp. On "Superalloys (Superalloys 1996)," (ed R.D. Kissinger et. al), 101-110; 1996, Warrendale, P.A., The Minerals, Metals & Materials Society, Seven Springs.

[12] Zhang, H.R., Ghoneim, A. and Ojo, O.A., "TEM Analysis of Diffusion Brazement Microstructure in a Ni3Al-based Intermetallic Alloy," Materials Science, Vol. 46, (2011), pp. 429-437.

[13] Darolia, R., Labrman, D.F. and Field, R.D., "Formation of Topologically Closed Packed Phases in Nickel Base Single Crystal Superalloys," Superalloys 1988, (ed. S. Reichman, D.N. Duhl, G. Maurer, S. Anolovich and C. Lund), pp. 255-264, 1988, The metallurgical Society.

[14] Durand-Charre, M., The Microstructure of Superalloys, Gordon and Breach Science Publishers (1997), pp.71-72.

[15] Zhao, S., Xie, X., Smith, G.D. and Patel, S.J., "Research and Improvement on Structure Stability and Corrosion Resistance of Nickel-Base Superalloy Inconel Alloy 740," Vol. 27, (2006), pp.1120-1127.